Journal of Drug Delivery Science and Technology 115 (2026) 107762

Contents lists available at ScienceDirect

Journal of Drug Delivery Science and Technology

journal homepage: www.elsevier.com/locate/jddst

Investigation of solid-state forms between *p*-aminosalicylic acid and adenine: Exploring salts, cocrystals and their polymorphism

Beatrice Maiorca [a], Chiara Sabena [a], Emanuele Priola [a], Ilenia D'Abbrunzo [b], Beatrice Perissutti [b], Roberto Gobetto [a,*], Michele R. Chierotti [a,**]

[a] Department of Chemistry, University of Torino, Via Pietro Giuria 7, 10125, Torino, Italy
[b] Department of Chemical and Pharmaceutical Sciences, University of Trieste, P.le Europa 1, 34127, Trieste, Italy

ARTICLE INFO

Keywords:
P-aminosalicylic acid
Adenine
Cocrystals
Molecular salts
Solid-state NMR
Polymorphism
pK_a rule

ABSTRACT

This study investigates the polymorphic behavior of multi-component adducts formed between *p*-aminosalicylic acid (PAS), a second-line anti-tuberculosis drug, and adenine (ADE), a hydrogen bond-rich coformer. Given a ΔpK_a of 2.2 between PAS and ADE, within the salt–cocrystal uncertainty region, three distinct solid-state forms (an anhydrous and two hydrates) were synthesized via solvent-tuned liquid-assisted grinding and solution evaporation. Comprehensive characterization was performed using solid-state NMR, FT-IR and Raman spectroscopy, X-ray diffraction (SCXRD and PXRD), DSC, TGA, and *in vitro* dissolution tests. Results revealed significant differences in structure, hydrogen-bonding networks, and thermal properties among the forms, with PAS:ADE stoichiometries of 3:2 for the anhydrous form and 1:1 for the hydrated forms. These findings demonstrate the critical role of solvent and stoichiometry in directing adduct formation and polymorphism, offering insights for optimizing drug formulation and expanding intellectual property strategies in pharmaceutical development.

1. Introduction

Polymorphism, *i.e.*, the ability of a substance to adopt different arrangements or conformations of the molecules in the crystal lattice [1], extends from single-component to multi-component systems. This phenomenon is a crucial aspect of solid-state chemistry, particularly in the pharmaceutical field, where different solid forms can have a significant impact on drug properties [2–7]. Indeed, polymorphs of an Active Pharmaceutical Ingredient (API) or its multi-component adducts can exhibit substantial differences in their physical and chemical properties, such as stability, solubility, dissolution rate, and bioavailability [2,8,9]. These variations directly influence drug performance, affecting not only efficacy but also manufacturability, shelf life, and regulatory approval [10–13]. Since regulatory agencies, including the Food and Drug Administration (FDA) and the European Medicines Agency (EMA), recognize different polymorphs of a drug as distinct entities in patent submissions, the ability to identify and control polymorphism has become a key aspect for pharmaceutical development [12,14].

Among the various crystal forms, multi-component adducts, such as salts and cocrystals, represent a promising strategy for modulating and optimizing the solid-state properties of an API [15]. In particular, pharmaceutical cocrystals represent a more recent approach that is attracting significant interest from pharmaceutical companies. Indeed, cocrystals are crystalline materials composed of two or more distinct molecules, typically an API and a coformer, that are held together through non-covalent neutral interactions, *e.g.*, hydrogen bonds, van der Waals forces, or π-stacking interactions, in the same crystal lattice [16–18]. Thus, unlike salts, cocrystals do not involve a proton transfer between the components, allowing their formation even with weakly ionizable or non-ionizable molecules [15]. This makes cocrystals a versatile and valuable tool for achieving desirable changes in their solid-state properties and overcoming physicochemical properties issues.

The control and prediction of salt/cocrystal formation remains a challenge. Indeed, it is well known that polymorphic outcomes can be highly sensitive to crystallization conditions, *e.g.* solvent, temperature, and synthetic technique, making the production of a desired polymorph difficult to reproduce [5,19,20]. Recent developments in continuous

* Corresponding author.
** Corresponding author.
E-mail addresses: roberto.gobetto@unito.it (R. Gobetto), michele.chierotti@unito.it (M.R. Chierotti).

https://doi.org/10.1016/j.jddst.2025.107762
Received 31 July 2025; Received in revised form 17 October 2025; Accepted 7 November 2025
Available online 8 November 2025

crystallization processes aim to address these challenges by offering more controlled crystallization environments, minimizing batch-to-batch variability and improving reproducibility of polymorphic forms [20,21]. For instance, the most widespread approach to control the polymorph formation is through the use of different solvents in supramolecular syntheses [22]. Traditionally, the formation of an adduct as a salt or a cocrystal is predicted using the empirical "ΔpK_a rule", which states that a proton transfer is expected to occur if the difference between the pK_a values of the protonated base and the acid ($\Delta pK_a = pK_a$ of the protonated base $- pK_a$ of the acid) exceeds a certain threshold, typically around 3 or 4 [23]. However, several studies have demonstrated that this rule includes a region of uncertainty, when ΔpK_a falls within the range of −1 to 4, where the probability to obtain a salt or a cocrystal is extremely similar [24–26]. Rather than being a limitation, this region of uncertainty is of particular interest, since it enables to obtain different solid-state forms from the same pair of molecules. By selecting coformers with appropriate pK_a values to achieve a ΔpK_a within this region and by carefully tuning crystallization and synthesis conditions, one can selectively access either salt or cocrystal forms, expanding opportunities to tailor pharmaceutical properties and optimize intellectual property strategies [24]. Despite its potential, this region remains only partially explored. The very limited number of reported cases already reveals a notable diversity of outcomes, ranging from distinct salt and cocrystal forms with the same stoichiometry (*i.e.*, salt/cocrystal polymorphism) [8,9,27–30] to adducts differing in stoichiometric ratio or solvation [31–33]. The scarcity of systematically investigated examples hampers the development of general principles to rationalize proton transfer and solid-form selection within this uncertainty window. Thus, a broader and well-characterized set of case studies is essential to elucidate governing factors and enhance predictive capability.

Furthermore, the characterization of solid forms falling within this ΔpK_a uncertainty range poses further challenges. The subtle differences between salts, cocrystals, and their polymorphs can be difficult to detected when using a single analytical technique. Consequently, a comprehensive understanding requires an integrated multi-technique approach combining complementary methods. Classical methods such as single-crystal and powder X-ray diffraction (SCXRD and PXRD) offer direct insight into molecular packing, long-range order, and structural elucidation [34–40]. More recently, vibrational spectroscopies, particularly Raman and terahertz (THz) spectroscopy, have been widely applied as non-destructive probes of hydrogen-bonding environments, lattice dynamics, and, when combined with modeling, indicators of ionic vs neutral character in pharmaceutical solids [41–46]. Indeed, they are especially sensitive to low-frequency phonon modes and intermolecular vibrations, enabling reliable polymorph discrimination and the identification of supramolecular synthons in pharmaceutical multicomponent adducts [37,44,45,47–49]. Moreover, solid-state NMR (SSNMR) spectroscopy, due to its sensitivity to subtle variations in the electronic environment, allows for accurate localization of hydrogen atoms along hydrogen bonds, which is crucial for differentiating between salt and cocrystal forms [8,9,37,50–53]. Taken together, these techniques provide complementary insights essential for developing a comprehensive understanding of pharmaceutical multicomponent systems, especially in the presence of polymorphism, solvation, and protonation-state ambiguities.

This work focused on adducts obtained from *p*-aminosalicylic acid (PAS) and adenine (ADE), whose molecular structures are reported in Scheme 1. PAS is a well-known second-line API in the treatment of multidrug-resistant tuberculosis (MDR-TB). According to the Biopharmaceutical Classification System (BCS), PAS falls between classes II and IV due to low solubility in aqueous solutions [54]. Furthermore, the compound is susceptible to irreversible decarboxylation under acidic conditions [55], heat exposure, or moisture, resulting in the formation of *m*-aminophenol, a substance known for its toxicity [56,57]. Goswami et al. have been actively engaged in studying the interactions of new

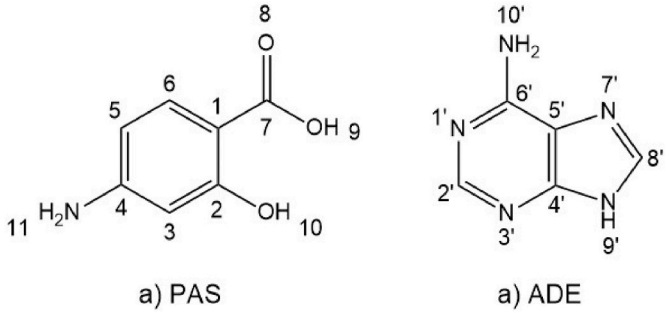

Scheme 1. Molecular structures of (a) PAS and (b) ADE, with atom numbering.

forms of PAS cocrystals with pyridine and its derivatives, to overcome these problems [58,59]. ADE was strategically chosen as a coformer primarily based on the ΔpK_a rule. The pK_a of the basic nitrogen N1' of ADE is 4.2,[60] while the pK_a of the carboxylic group in PAS is 2.0 [61], giving a ΔpK_a of 2.2, value which falls within the uncertainty region. Moreover, ADE is a versatile coformer due to its ability to form multiple hydrogen bonds, attributed to the presence of several additional hydrogen-bond donor and acceptor sites in its molecular structure (Fig. 1) [33,62]. In addition, from a biocompatibility perspective, although ADE is not classified as a Generally Recognized as Safe (GRAS) substance by the FDA, it is present in significant quantities in many foods intended for human consumption [63]. ADE is known to form crystalline adducts with molecules that exhibit carboxylic functionality, such as salicylic acid [33], benzoic acid [64] and oxalic acid [65]. ADE solvates have also been reported [64].

Based on this evidence, PAS and ADE were considered ideal candidates for the present research study [33].

Here, we report a comprehensive characterization that allowed to detect and precisely assess three new distinct solid forms of the PAS-ADE adduct obtained by varying the synthesis conditions and the solvent: an anhydrous form (Form A) with 3:2 stoichiometry, and two hydrated forms (Forms B and C) with 1:1 stoichiometry. Their polymorphic behavior, molecular packing, ionic or neutral character, thermal stability and dissolution behavior were investigated using a combination of

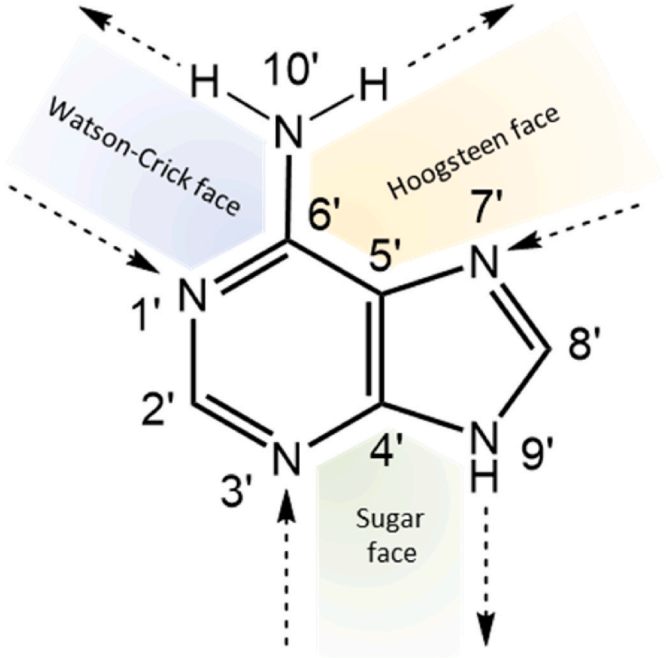

Fig. 1. The possible hydrogen bond interactions of adenine through the Watson-Crick, Hoogsteen, and Sugar faces [33].

complementary techniques, *i.e.*, solid-state NMR (SSNMR), Fourier-Transform Infrared (FT-IR) and Raman spectroscopies, Single-Crystal and Powder X-Ray Diffraction (SCXRD and PXRD), Differential Scanning Calorimetry (DSC) and Thermogravimetric Analysis (TGA), as well as *in vitro* dissolution tests.

2. Materials and methods

PAS (purity 99%), ADE (purity >99%) and all used solvents were purchased from Sigma-Aldrich. All the starting materials were used for the preparation of adducts without further purification.

2.1. Synthesis of adducts

The syntheses of the adducts were carried out using liquid-assisted grinding (LAG). To achieve complete conversion of the starting materials, LAG time and the stoichiometric ratios of the adducts were optimized. The optimization process involved monitoring the reactions every 10 min by FT-IR ATR and Raman spectroscopy. For more complex stoichiometries, such as the 3:2 PAS:ADE ratio of Form A, SSNMR was essential for detecting the excess of unreacted ADE and driving the synthesis toward the correct stoichiometry. The reproducibility of the syntheses was confirmed by three independent batches for each form, all exhibiting superimposable FTIR-ATR and ^{13}C SSNMR spectra.

2.1.1. Form A: Anhydrous cocrystal of PAS-ADE [$(ADE)_2 \cdot (PAS)_3$)]

A white powder was obtained by LAG technique: 170 mg (1.11 mmol) of PAS and 100 mg (0.74 mmol) of ADE were manually ground with 5 drops of acetonitrile (85 μL; η = liquid (μL)/sample (mg) = 0.3)[20] added every 10 min for 1 h and 30 min.

2.1.2. Form B: Hydrate salt of PAS-ADE ($ADE^+PAS^- \cdot 2H_2O$_B)

A white powder was obtained by LAG technique: 120 mg (0.78 mmol) of PAS and 105.9 mg (0.78 mmol) of ADE were manually ground with 5 drops of deionized water (125 μL; η = 0.5) added every 10 min for 30 min.

Crystals, suitable for SCXRD, were obtained by the slow solvent evaporation technique: 34 mg of PAS (0.22 mmol) and 30 mg of ADE (0.22 mmol) were dissolved in deionized water (2 ml). The solubilization of the starting materials was facilitated by stirring and heating (T = 50–80 °C).

2.1.3. Form C: Hydrate salt of PAS-ADE ($ADE^+PAS^- \cdot 2H_2O$_C)

A white powder was obtained by LAG technique: 120 mg (0.78 mmol) of PAS and 105.9 mg (0.78 mmol) of ADE were manually ground with 5 drops of a 1:1 (v/v) mixture of ethanol and deionized water (100 μL; η = 0.4) every 10 min for 30 min.

Crystals, suitable for SCXRD, were obtained by the slow solvent evaporation technique: 34 mg of PAS (0.22 mmol) and 30 mg of ADE (0.22 mmol) were dissolved in a 1:1 (v/v) mixture of ethanol and deionized water (2 ml). The solubilization of the starting materials was facilitated by stirring and heating (T = 50–80 °C).

2.2. Characterization techniques

2.2.1. FT-IR ATR spectroscopy

FT-IR spectra were recorded on an Equinox 55 (Bruker) spectrometer with an ATR reflectance attachment. Spectra were collected in the 400–4000 cm^{-1} range with a resolution of 4 cm^{-1} and 16 scans.

2.2.2. Raman spectroscopy

Raman spectra were registered with a Bruker Vertex 70 instrument (Bruker, Billerica, MA, USA), equipped with a RAM II module. An excitation source at 1064 nm was used, with a laser power between 10 and 50 mW and a number of scans between 80 and 500, depending on the analyzed sample, with a resolution of 4 cm^{-1}. The employed spectral range is comprised between 50 and 4500 cm^{-1}, using a CaF_2 beam splitter.

2.2.3. Powder X-ray diffraction

PXRD patterns were recorded on an Xpert Pro (45 kV, 40,000 μA) diffractometer in the Bragg-Brentano geometry, using Cu-Kα radiation (λ = 1.5418 Å) in the 2θ range between 5° and 50° (continuous scan mode, step size 0.0167°, counting time 40 s).

2.2.4. Single-crystal X-ray diffraction

SCXRD analyses were performed on selected single-crystal samples. Single crystal data were collected on a Gemini R Ultra diffractometer (Agilent Technologies UK Ltd., Oxford, U.K.) using a graphite-monochromatic Cu Kα radiation (l = 1.5406 Å) with the w-scan method. The copper-derived radiation was preferred for the cases of very weakly diffracting crystals. The CrysAlisPro software was used for retrieving cell parameters, for performing data reduction, and for the absorption correction (with multi-scan technique). All structures were solved by direct methods using ShelXS-14 [66] and refined with full-matrix least-squares on F2 using SHELXL-14 [67] and the Olex2 program [68]. All non-hydrogen atoms were anisotropically refined. Hydrogen atoms were calculated and riding on the corresponding atom. Structure images were obtained using the Mercury software [69,70]. Crystal data and refinement, selected bond lengths, and angle amplitudes are reported in the Supplementary material (Table S1–S5). The crystallographic data for the crystallized compounds were deposited within the Cambridge Crystallographic Data Centre as supplementary publications under the CCDC numbers 2447188 and 2447189. This information can be obtained free of charge from the Cambridge Crystallographic Data Centre via www.ccdc.cam.ac.uk/data_request/cifcodeCCDC.

2.2.5. Hirshfeld surface and energy framework analyses

The Hirshfeld surface analysis, and calculations of intermolecular interaction energies and energy frameworks were performed by using Mercury [69,70] and CrystalExplorer17 suites [71–74]. All the results are reported in the SI. The B3LYP/6-311G(d,p) method, as implemented in the Mercury and CrystalExplorer17 programs, was used to calculate pairwise interaction energies.

2.2.6. Solid-state NMR

The ^{13}C CPMAS SSNMR spectra of Form A, B, and C, as well as the ^{15}N CPMAS SSNMR spectrum of Form A, were recorded at room temperature using a Bruker Avance II 400 Ultra Shield spectrometer. The spectrometer operated at 400.23, 100.63, and 40.56 MHz for ^{1}H, ^{13}C, and ^{15}N, respectively. The powder samples were packed into 4 mm o.d. zirconia rotors without further preparation. The ^{13}C and ^{15}N CPMAS spectra were acquired at spinning speeds of 12 kHz and 9 kHz respectively, using a ramp cross-polarization pulse sequence. A 90° ^{1}H pulse of 3.80 μs and a two-pulse phase modulation (TPPM) decoupling scheme with a radiofrequency field of 69.4 kHz were employed. The contact time was set to 3 ms for ^{13}C and 4 ms for ^{15}N spectra. Optimized recycle delays of 30 s for Form A, of 15.2 s for Form B, and of 60 s for Form C, and a number of scans from 44 to 140 for the ^{13}C CPMAS spectra, and 24710 scans for the ^{15}N CPMAS spectrum of Form A were used. The ^{13}C and ^{15}N chemical shift scales were calibrated using γ-glycine as a secondary external standard, with the ^{13}C methylene peak at 43.7 ppm and the ^{15}N peak at 33.4 ppm (referenced to liquid NH_3).

^{1}H-^{13}C 2D CP FSLG HETCOR measurements were acquired on the same spectrometer at a spinning speed of 12 kHz, with a contact time of 0.1 or 2.5 ms to allow only short-range or also long-range magnetization transfer, respectively. FSLG homonuclear decoupling was applied during t_1. For each spectrum, a two-pulse phase modulation (TPPM) decoupling scheme was used, with a radiofrequency field of 69.4 kHz.

The ^{13}C CPMAS SSNMR spectra of Form B and C after heating and ^{15}N CPMAS SSNMR spectra of Form B and C and were collected using a

Jeol ECZR 600 instrument, operating at 600.17, 150.91 MHz and 60.82 MHz for ^{1}H, ^{13}C and ^{15}N nuclei, respectively. The powder samples were packed directly into 3.2 mm zirconia rotors without further preparation. The ^{13}C spectra were recorded at room temperature at a spinning speed of 20 kHz, employing a ramped cross-polarization pulse sequence with a 90° ^{1}H pulse of 2 μs, a contact time of 3.5 ms, and optimized recycle delays of 37.3 s for Form B and 32.6 s for Form C. The ^{15}N spectra were recorded at room temperature at a spinning speed of 9 kHz, employing a ramped cross-polarization pulse sequence with a 90° ^{1}H pulse of 2.5 μs, a contact time of 7 ms, and optimized recycle delays of 18.7 s for Form B and 76.2 s for Form C. A number of scans of 400 for the ^{13}C CPMAS spectra and of 6460 (for Form C) and 28510 (for Form B) for ^{15}N CPMAS SSNMR was used. The TPPM decoupling scheme was used, with a radiofrequency field of 125 kHz and 100 kHz for ^{13}C and ^{15}N spectra, respectively. The ^{13}C and ^{15}N chemical shift scales were calibrated using the signal of external standard γ-glycine (^{13}C methylenic peak at 43.7 ppm and ^{15}N peak at 33.4 ppm with reference to liquid NH_3).

The ^{13}C T_1-^{1}H analysis, 10 spectra were acquired for 200 scans with different relaxation delays, included in the range 0.1–400 s and calculated by the Delta v5.2.1 software through an exponential algorithm. The spectra were acquired at a spinning speed of 20 kHz at probe temperature using a ramp cross polarization pulse sequence with a 90° ^{1}H pulse of 2 μs and a contact time of 3.5 ms.

2.2.7. Differential Scanning Calorimetry

DSC analyses were performed on the raw materials and each adduct sample. Accurately weighed amounts (2–4 mg) were introduced into 40 μL sealed and pierced aluminum crucibles and analyzed using a Mettler Toledo DSC 3 Star System (Milan, Italy) equipped with STAR^{e} software. The heating program ranged from 30 to 380 °C at 10 °C/min, under a nitrogen atmosphere with a flow rate of 50 mL/min.

2.2.8. Thermogravimetric Analysis

TGA measurements were performed over a temperature range of 25–400 °C under a 100 mL/min N_2 flow, on a Q600 SDT TA Instruments equipped with a DSC heat flow analyzer. Samples (approximately 10 mg of weight) were placed in alumina crucibles and heated with a ramp of 5 °C/min.

2.2.9. In Vitro Dissolution Tests

Prior to dissolution, solubility measurements of raw PAS were carried out by adding an excess amount (approximately 50 mg) of the drug to 5 mL of phosphate buffer (pH 7.4) and maintaining the suspension in a thermostated bath at 37 °C under agitation for 2 h. The solution was then filtered through a 0.45 μm membrane filter. The solubility of PAS at pH 7.4 was found to be 8.15 ± 0.015 g/L (mean ± S.D., n = 3), in agreement with literature data [56].

For the *in vitro* dissolution test, each experiment was performed using 150 mL of pH 7.4 phosphate buffer solution, according to ref [56], in a vessel directly connected to a thermostatic bath (37 °C), with a constant agitation provided by a magnetic stirrer. 3 mg of pure PAS or an equivalent PAS amount from each adduct (calculated based on the stoichiometry: Form A 3:2, Form B 1:1, Form C 1:1) was added to the dissolution medium ensuring sink conditions (C < 0.2 Cs). The experiment lasted for 1 h, and the absorbance was measured *in situ* through a fiber optic apparatus (HELLMA, Italy) connected to a spectrophotometer (ZEISS, Germany). The absorbance values were recorded at 299 nm (not overlapping with ADE, whose maximum absorption falls within the same spectral range as PAS. A Tyndall – Rayleigh scattering correction was applied to the recorded spectra to exclude the scattering occurring at every wavelength of undissolved particles. The results are reported as the average of three replicates, with standard deviations not exceeding 5% of the mean value.

3. Results and discussion

The PAS–ADE system yielded three distinct solid forms, depending on the synthetic method and solvent employed. The syntheses of the three adducts were carried out using both neat grinding (NG) and LAG [75] at room temperature, employing various solvents (Table 1). Only a few of the tested solvents enabled the selective formation of pure adducts: specifically, acetonitrile, ethanol, methanol and isopropanol yielded Form A, deionized water led to Form B, and a 1:1 (v/v) mixture of ethanol-deionized water or methanol-deionized water was effective for Form C. In contrast, NG and the remaining solvents listed in Table 1 resulted in heterogeneous mixtures of the starting materials.

Form A is an anhydrous cocrystal with a stoichiometric ratio of 3:2 (PAS:ADE), whereas Form B and C are hydrated salts, both with a 1:1:2 stoichiometric ratio (PAS:ADE:H_2O). As shown in Table 1, the absence of a solvent or the use of apolar/low-polarity solvents results in a mixture of the starting materials, whereas solvents with a higher dipole moment promote the formation of the three forms [22,76,77]. Form A is obtained with anhydrous high-dipole-moment solvents, while Form B and C are achieved when water or aqueous mixtures are used, leading to its incorporation into the crystal lattice and the formation of two polymorphic solvate adducts [78]. Thus, the solvent, whether protic/aprotic, seems not to affect the ionic/neutral character of the resulting product but, rather it allows or not its formation and hydration state (anhydrous or dihydrate).

The formation and key properties of these adducts were unequivocally confirmed and thoroughly characterized by a combination of techniques, including FTIR-ATR (see below **FT-IR ATR and Raman spectroscopy Analysis**), Raman spectroscopy (see below **FT-IR ATR and Raman spectroscopy Analysis**), PXRD (Fig. S3 in the Supplementary material), SCXRD (see below **Crystal structure Analysis** for Form B and C), SSNMR (see below **Solid-state NMR Characterization)**, Thermal analysis (see below **Thermal Analysis**) and in *vitro* dissolution testing (see below ***In Vitro Dissolution Tests***). Despite extensive attempts with different techniques and solvents, suitable single crystals of Form A for SCXRD analysis could not be obtained, due to the solubility properties of ADE, which is highly soluble in water and only sparingly soluble in organic solvents [79]. Slow evaporation of aqueous solutions of PAS and ADE invariably led to hydrated adducts, whereas experiments in organic solvents resulted in rapid precipitation and exclusively microcrystalline powders.

3.1. FT-IR ATR and Raman spectroscopy analysis

FT-IR ATR and Raman spectra of PAS, ADE, and the three adducts were acquired as a preliminary screening tool (Fig. 2; full-range spectra are reported in the Supplementary material, Fig. S1 and S2). As a representative example, Fig. 2 shows the corresponding spectra, where the characteristic FT-IR bands at 3493 and 3385 cm^{-1} (PAS) and 1671 cm^{-1} (ADE), together with the Raman peaks at 1126 (ADE) and at 1664 and 786 cm^{-1} (PAS), disappear or strongly decrease in the adducts, confirming the formation of new solid forms. Moreover, the spectral comparison clearly distinguishes three different adducts (Form A, B, and C) [80].

Examination of the Raman spectra (Fig. 2b) reveals that Form A exhibits characteristic peaks at 1486 and 1251 cm^{-1} (purple rectangular shadows) of the neutral N9′H tautomer as in pure ADE. In contrast, in Form B and C, these peaks disappear, indicating the presence of the N1′H^{+} cationic tautomer of ADE [60,81,82].

FT-IR ATR spectra (Fig. 2a) highlight the presence of water in Form B and C, as evidenced by the broad bands around 3000 cm^{-1} (cyan rectangular shadow), which are absent in Form A. Moreover, the modification of the PAS carbonyl C=O stretching band at 1609 cm^{-1} (red rectangular shadow) suggests the salification of Form B and C, while in Form A this peak remains substantially unaltered [83].

This primary investigation, together with SCXRD analysis (see

Table 1
Adducts obtained through NG (first line) and LAG, and their stoichiometric ratios. Each test was analyzed by FTIR-ATR (data not shown).

SOLVENT	OUTCOME PAS-ADE	STOICHIOMETRIC RATIO PAS:ADE
-	SM[a] heterogeneous mixture	-
acetonitrile	**FORM A**	3:2
methanol	**FORM A**	3:2
ethanol	**FORM A**	3:2
isopropanol	**FORM A**	3:2
tetrahydrofuran	SM[a] heterogeneous mixture	-
chloroform	SM[a] heterogeneous mixture	-
ethylacetate	SM[a] heterogeneous mixture	-
hexane	SM[a] heterogeneous mixture	-
deionized water	**FORM B**	1:1
mixture 1:1 (v/v) methanol/deionized water	**FORM C**	1:1
mixture 1:1 (v/v) ethanol/deionized water	**FORM C**	1:1

[(a)] SM = Starting Materials

(a) SM = Starting Materials.

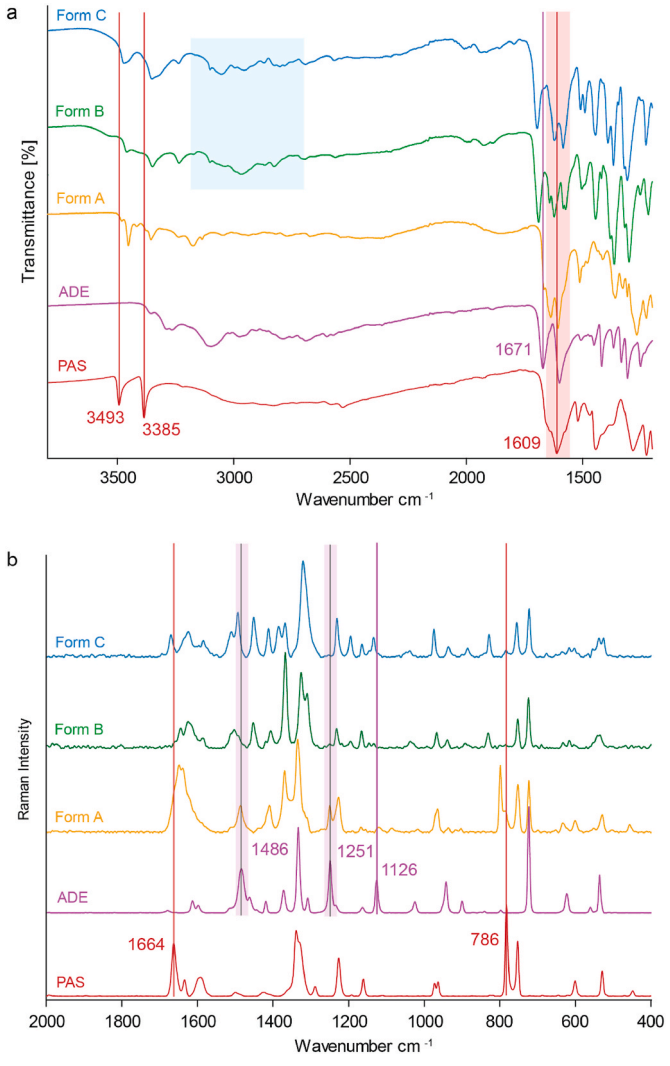

Fig. 2. Comparison of (a) enlarged view FT-IR ATR (3800–1200 cm^{-1}) and (b) enlarged view baseline-corrected Raman (2000–400 cm^{-1}) spectra of PAS, ADE, and the three adducts (Form A, B, and C). For the whole FT-IR ATR and Raman spectra see Supplementary material, Fig. S1 and S2.

Crystal Structure Analysis) and SSNMR characterization (see **Solid-State NMR Characterization**), confirms the formation of supramolecular adducts and provides insight into their structural nature.

3.2. *Crystal Structure Analysis*

The comparison between experimental and simulated PXRD patterns of Form B and C (Fig. S4 in the Supplementary material) confirmed that the single-crystal structures are representative of the bulk materials. Form B crystallizes in the non-centrosymmetric orthorhombic space group type *Fdd*2, while Form C adopts the centrosymmetric triclinic space group type *P*-1. Both contain one molecule each of ADE and PAS, along with two water molecules in the asymmetric unit, as confirmed by SSNMR (see below **Solid-state NMR Characterization**). Their hydrogen-bonding networks (Fig. 3a and b) are complex, involving all available hydrogen bond donors and acceptors through the Watson-Crick, Hoogsteen, and sugar faces. Both structures feature the expected O···H···N hydrogen bond between the COOH of PAS and the N1' of ADE consistent with the considered ΔpK_a. The C-O bond lengths in PAS (1.263/1.277 Å for Form B and 1.259/1.278 Å for Form C) along with the presence of a hydrogen electron density positioned close (<1.1 Å) to the N5 atom of ADE indicate the ionic nature of the adducts, *i.e.* salt formation, further confirmed by ^{13}C and ^{15}N SSNMR analysis (see below **Solid-state NMR Characterization**). The ionic character of the two coformers significantly influences both the nature and strength of the intermolecular interactions in the two crystal forms.

In both structures, ADE and PAS strongly interact through charge-assisted π···π stacking (Fig. 4a and b) forming columns with the sequence $PAS^-\cdots ADE^+\cdots PAS^-\cdots ADE^+$, and through strong inter-columnar charge-assisted hydrogen bonds (Fig. 4c). As expected, neighboring columns are staggered to maximize favorable anion-cation and minimize repulsive anion-anion and cation-cation contacts. The main differences between the two forms are as follows: a) in Form B, the columns are not parallel (inter-columnar angle = 21.57°), whereas in Form C, the molecules lie in coplanar arrangements forming layers linked by water molecules (Fig. S5 in the Supplementary material); b) the role of water differs: in Form B, water molecules bridge different columns (Fig. 3a), whereas in Form C, they connect the layers by linking molecules within the same column (Fig. 3b). In both forms, water molecules are located within channels surrounding the $PAS^-\cdots ADE^+$ columns (Fig. 3c and d). However, their weak polarization via hydrogen bonding contributes only marginally to the overall lattice energy, as shown by intermolecular interaction energy calculations (Fig. 4d and Fig. S6–S11 in the Supplementary material). In Form B, the two water molecules differ in their hydrogen-bonding interactions, one being

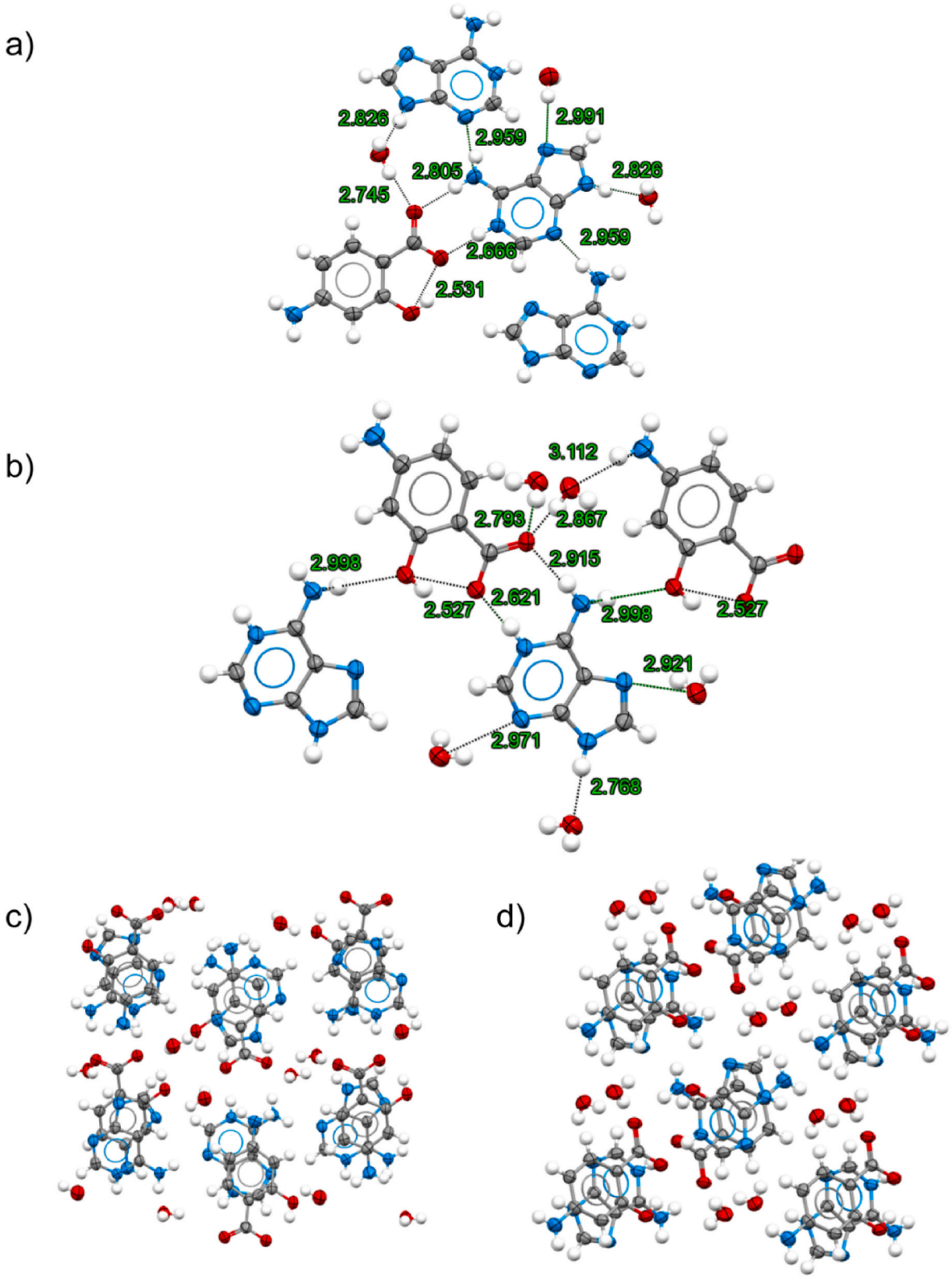

Fig. 3. Fragments of the crystal packing of Form B (a and c) and of Form C (b and d) (Ellipsoid probability: 70%). Color code: grey, carbon; blue, nitrogen; red, oxygen; white, hydrogen. (For interpretation of the references to color in this figure legend, the reader is referred to the Web version of this article.)

weakly and the other strongly bonded, while in Form C, their bonding energies are similar (Fig. S12 in the Supplementary material).

Regarding the overall stabilization, the dominant contribution is electrostatic, as expected for salt adducts. Despite the presence of aromatic moieties, the dispersion component is negligible (see Energy Frameworks and intermolecular contacts in Tables S6 and S7 and Fig. S6–S11 in the Supplementary material). Furthermore, the repulsive $PAS^{-}\cdots PAS^{-}$ and $ADE^{+}\cdots ADE^{+}$ interactions between adjacent columns also contribute to the crystal packing and are minimized by the aforementioned columnar staggering (see yellow components in Fig. S6, S7,

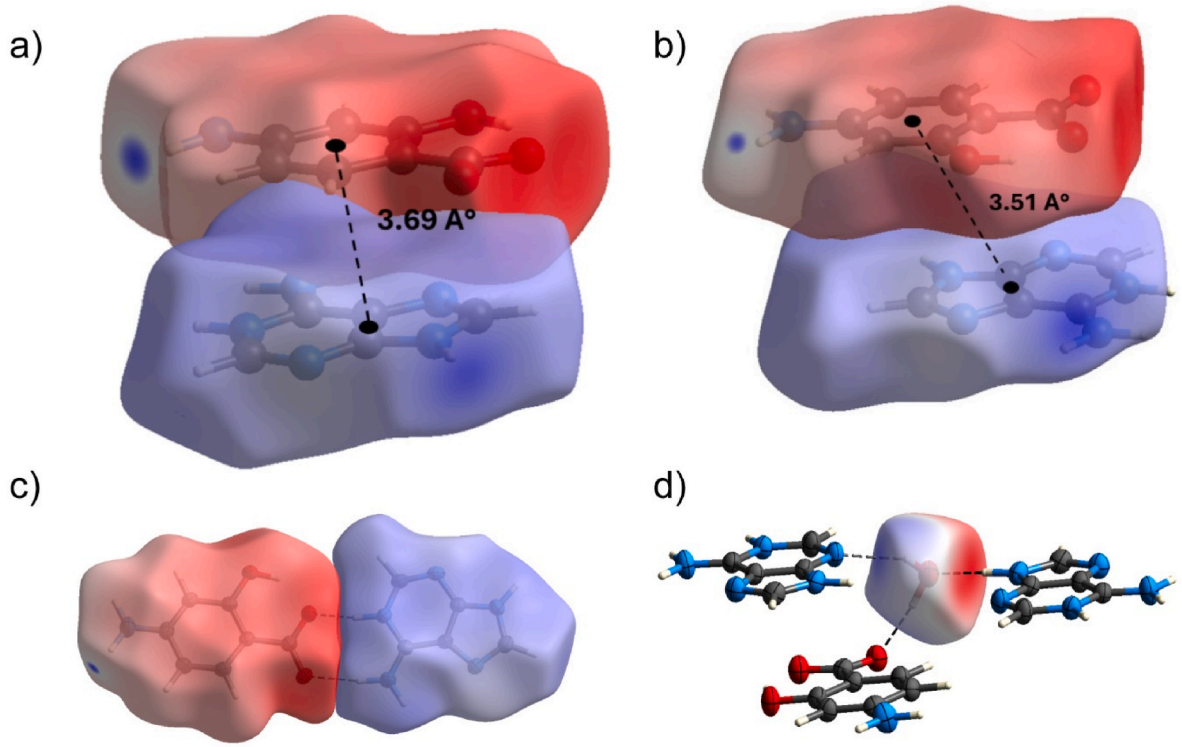

Fig. 4. Electrostatic potential projected on the Hirshfeld surface for the charge-assisted π···π stacking fragment in Form B (a) and in Form C (b), charge-assisted hydrogen bond fragment (O-H···N1′ and N10′-H···O) (c) with distances of O-N1' = 2.666 (Form B) and 2.621 (Form C) and of N10′-O = 2.805 (Form B) and 2.915 (Form C), (d) and for the hydrogen bonded water. Color code: red, negative regions; blue, positive regions [74]. (For interpretation of the references to color in this figure legend, the reader is referred to the Web version of this article.)

S9 and S10 in the Supplementary material) [71–73].

3.3. Solid-state NMR characterization

All ^{13}C and ^{15}N CPMAS SSNMR spectra are reported in Fig. 5 and 6, respectively, while the chemical shifts are listed in Table S8 in the Supplementary material.

Form A contains three independent molecules of PAS and two of ADE (3:2 stoichiometry), as highlighted in the ^{13}C CPMAS spectrum by the presence of three signals (at 175.2, 174.3, and 173.3 ppm) attributable to C7 of PAS and two signals (at 119.2 and 117.3 ppm) assignable to C5′ of ADE (Fig. 5). The ^{13}C CPMAS spectra of Form B and C suggest the presence of one independent molecule of each component in both forms (*i.e.*, Z' = 1), confirming a 1:1 stoichiometry.

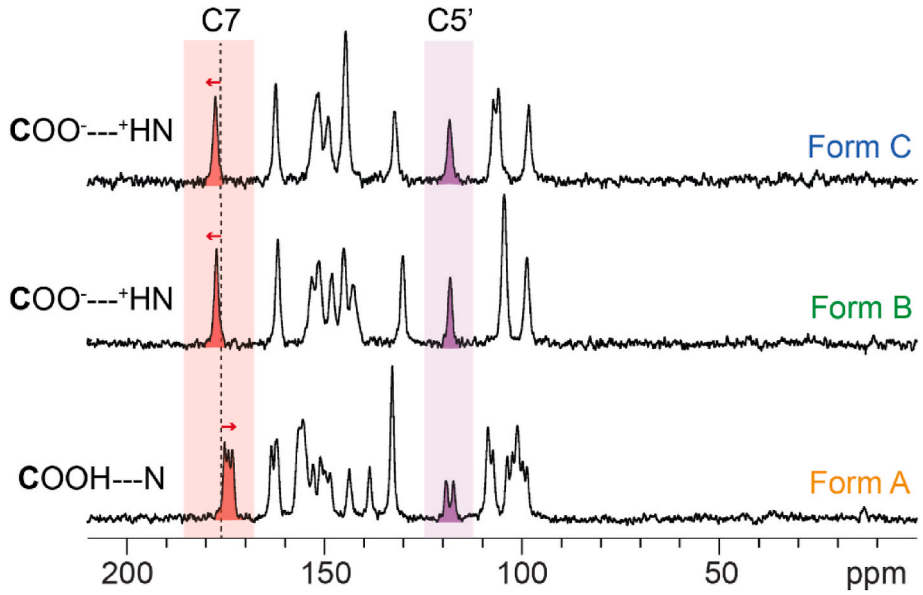

Fig. 5. ^{13}C (100.63 MHz) CPMAS SSNMR spectra of Form A, B, and C, acquired at a spinning speed of 12 kHz and room temperature. The black dashed line indicates the position of the COOH signal in the spectrum of pure PAS. Filled colored peaks correspond to signals assignable to PAS (red) and ADE (purple). (For interpretation of the references to color in this figure legend, the reader is referred to the Web version of this article.)

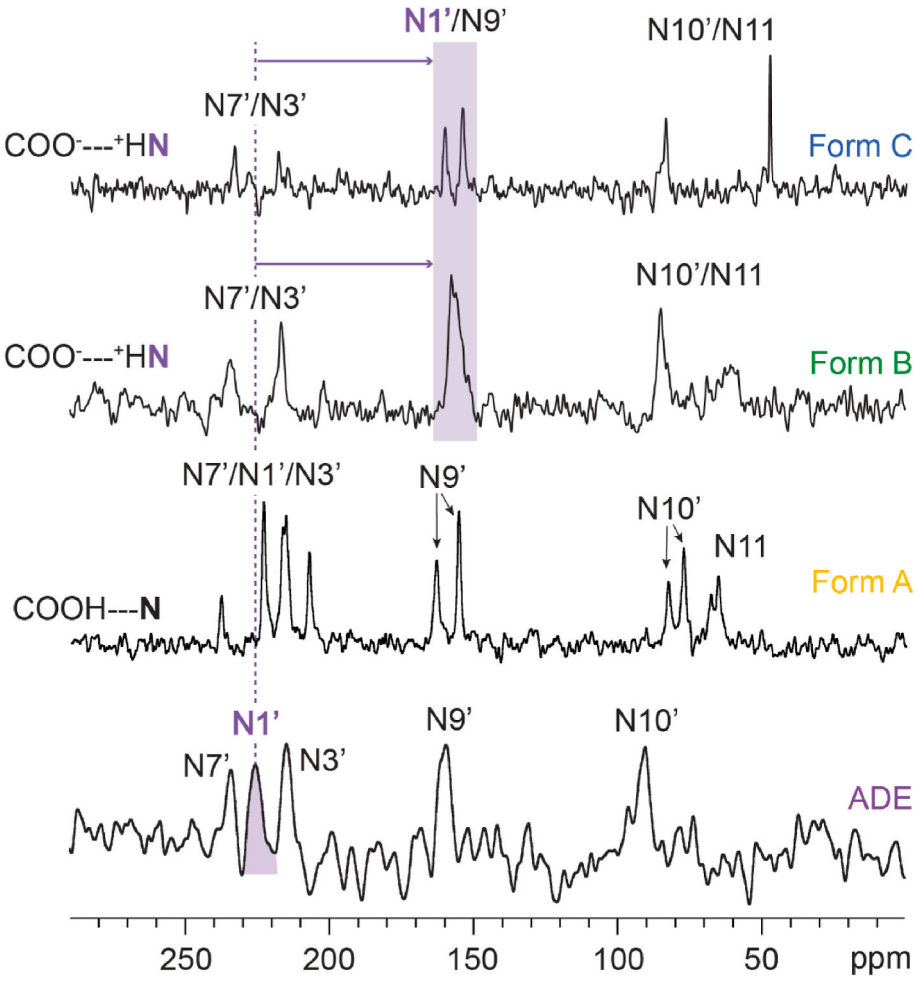

Fig. 6. ^{15}N (40.56 MHz) CPMAS SSNMR spectrum of ADE and Form A and ^{15}N (60.82 MHz) CPMAS spectra of Form B, and Form C, recorded at a spinning speed of 9 kHz and room temperature. The pyridinic-like N1′ signal of ADE is highlighted in purple to show the pronounced downfield shifts in Form B and C; by contrast, in Form A the N1′ signal falls within the 240–203 ppm range, with also N3′ and N7′ signals. (For interpretation of the references to color in this figure legend, the reader is referred to the Web version of this article.)

The chemical shift of the carboxylic group can be used to investigate the protonation state of the adducts [50]. For ^{13}C signals of carboxylic groups, hydrogen bond formation typically causes a high-frequency shift of about 3–7 ppm. When proton transfer occurs, resulting in a carboxylate group and a charge-assisted hydrogen bond, the shift reaches a maximum (around 6–7 ppm). However, very strong hydrogen bonds, such as those in cyclic COOH dimers, often show chemical shifts similar to those of carboxylate groups and this must be considered when analyzing the shift upon adduct formation. This is the case of PAS which exhibits the homodimerization of the COOH group [50]. As shown in Fig. 5, Form A exhibits a shift toward lower frequencies (from 176.3 ppm to 175.2, 174.3, and 173.3 ppm) compared to pure PAS, consistent with a neutral interaction. In contrast, a slight shift toward higher frequencies was observed for the C7 signal of the carboxylic group in Form B and C (from 176.3 ppm to 177.3 and 177.7 ppm, respectively), suggesting salt formation.

Key evidence of the ionic or neutral character of the adducts is provided by the ^{15}N CPMAS spectra. Indeed, aromatic ^{15}N nuclei are particularly sensitive to protonation, exhibiting shifts from 60 to 100 ppm toward lower frequencies [50].

In particular, in Form B and C, SCXRD analysis identified a supramolecular synthon wherein the carboxylic group of PAS interacts with the Watson-Crick face of ADE, directly involving N1′ in a charge-transfer N^{+}-H···O^{-} hydrogen bond (see above **Crystal Structure Analysis**). This evidence is supported by ^{15}N CPMAS spectra (full signal assignment discussed in Section S1 in the Supplementary material), where a signal, assigned to N1′ based on SCXRD data, shifts by almost 65–70 ppm to lower frequencies for both adducts (from 225.4 to 157.8/156 ppm for Form B and to 160.5/154.3 ppm for Form C, Fig. 6), corroborating the formation of salts. The assignment of N1′ as protonation site is further supported by its higher basicity compared to N7′ and N3′ as evidenced also through solution NMR studies on purine rings under acidic conditions [84]. In contrast, for Form A, the signals of N1′ are observed in the 240–203 ppm range, where N3′ and N7′ signals can also be detected (Fig. 6). Notably, even the signal at lowest frequencies (207.4 ppm) exhibits a limited deviation from that of pure ADE (225.4 ppm), thereby confirming the identification of this form as a cocrystal, as also indicated by the shift towards lower frequencies of the carboxylic group in the ^{13}C CPMAS spectra.

Since single crystals of Form A suitable for SCXRD could not be obtained, additional 2D "short-range" and "long-range" ^{1}H–^{13}C CP FSLG HETCOR experiments were performed to probe the hydrogen bond networks and refine the ^{13}C chemical shift assignment (Fig. S13 and S14 in the Supplementary material). The “short-range” HETCOR spectrum enabled precise identification of carbon atoms covalently bonded to hydrogen atoms. Interpretation of the long-range HETCOR spectrum was more challenging due to the five molecules in the asymmetric unit, yet it revealed that the carboxyl groups of the three PAS molecules participate in weak to moderate hydrogen bonds, as indicated by ^{1}H resonances at 15.73, 15.15, and 13.91 ppm [50]. Notably, the carboxylic

proton at 15.73 ppm correlates with C8′ and C5′ of ADE, both bonded to N7'. This supports the formation of a COO-H···N7' hydrogen-bonding synthon between PAS and the Hoogsteen face of ADE (Fig. S15 in Supplementary material), consistent with the ability of ADE to engage not only its most basic site, N1′, but also its additional acceptors, N7′ and N3′ [33].

3.4. Thermal Analysis

The starting materials and the three forms were analyzed by DSC and TGA (Fig. 7 and S16 in the Supplementary material). Form A shows no weight loss below 157 °C (TGA $T_{onset\text{-}PAS}$) when it starts to decompose, confirming its anhydrous nature. Form B and C, instead, exhibit a ~11% weight loss below 110 °C, consistent with the release of two water molecules from the crystal lattice. For Form B, TGA, DTG (first derivative of the TGA curve) and DSC analyses reveal two distinct dehydration events (Fig. 7c and d). Highlighted in the TGA analysis, it shows a steady loss (~5%) with a peak at 60 °C (T_{1w}) followed by a second loss (~5%) at 89 °C (T_{2w}) (Fig. 7d). In contrast, Form C exhibits a sharper endothermic peak in DSC and a corresponding weight loss at 95.3 °C (T_w) in TGA analysis (Fig. 7e and f). These observations are supported by SCXRD data, which show that both forms contain two water molecules in channel-like cavities [85]. In Form B, the crystallographic data reveal that one molecule is more weakly coordinated, while the other one participates in stronger hydrogen bonding (Fig. S12 in the Supplementary material). In Form C, the two water molecules participate in hydrogen bonds of comparable strength, consistent with the observed thermal behavior (Fig. S12 in the Supplementary material).

The TGA curve of PAS reveals a two-stage decomposition process, culminating in complete mass loss (100%). The first event, with an onset temperature (T_{onset}) of 146.3 °C (Fig. S16b in the Supplementary material), corresponds for approximately 30% of the total mass loss [86]. This observation could be related to CO_2 release, as this value is close to the theoretical CO_2 content in the API (28.7%). The TGA curves of the new forms reveal distinct onset temperatures for the first PAS weight loss ($T_{onset\text{-}PAS}$): 157 °C for Form A, 145 °C for Form B, and 155 °C for Form C (Fig. 7b–d and f). Additionally, in the adducts, a two-stage mass loss of PAS is evident, followed by the degradation of ADE at 313 °C ($T_{onset\text{-}ADE}$, Fig. 7b–d and f).

The DSC thermogram of PAS displays a melting endotherm with a peak temperature (T_m) at 146.3 °C, followed by a second endothermic event attributed to thermal degradation (Fig. S16a in the Supplementary material) [87]. In Form A, T_m occurs at 162.7 °C and appears as the sharpest peak among the three adducts (Fig. 7a). Form B, after

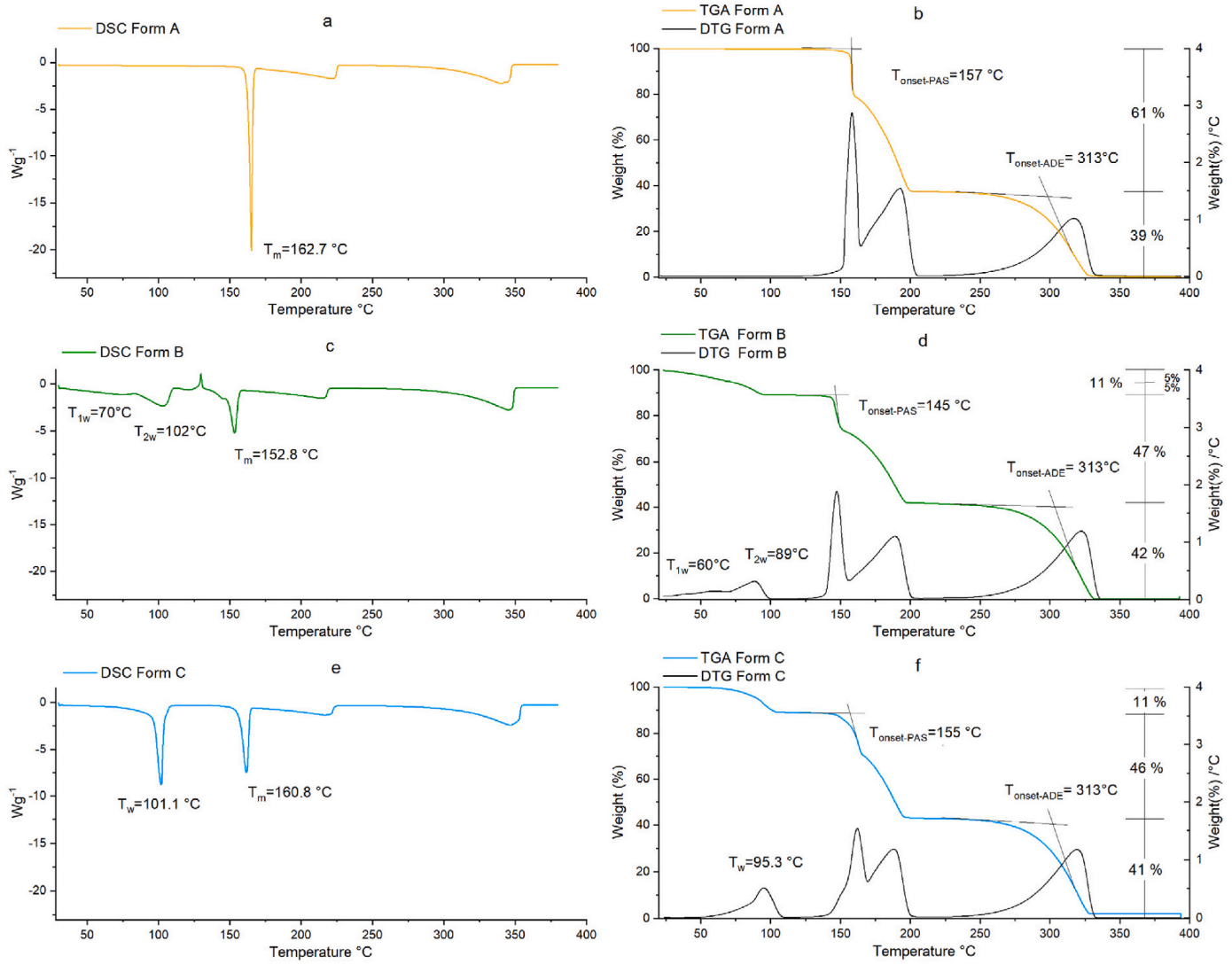

Fig. 7. DSC, TGA and DTG profiles of Form A (a,b), Form B (c,d), and Form C (e,f). DSC thermograms display melting temperatures (T_m), with temperature peaks dehydration events observed for Form B and C. TGA profiles show onset temperatures (T_{onset}), temperature peaks of dehydration and percentage weight losses consistent with the stoichiometry of the respective adducts.

dehydration, shows an exothermic recrystallization event, followed by a melting endotherm at 152.8 °C (Fig. 7c). In contrast, Form C does not exhibit any recrystallization, displaying a single endothermic peak at 160.8 °C (Fig. 7e). In all cases, PAS degradation occurs after melting, while ADE undergoes thermal degradation at 358.7 °C (Fig. 7a–c and e).

For a more detailed analysis, Form B and C were heated at 100 °C in an oven while being monitored by Raman spectroscopy and SSNMR. After 30 min of heating, both forms exhibited the same Raman and ^{13}C CPMAS SSNMR spectra (Fig. S17 and S18 in the Supplementary material), different from the starting forms (B and C), the starting materials and the anhydrous Form A (Fig. S19–S22 in the Supplementary material). This suggests the occurrence of water release and a complete conversion to the same product which seems to contain a small amount of a different phase as suggested by ^{1}H T_1 analyses (through ^{13}C signal). This highlights that the heating behavior in the oven, where both Form B and C yield the same product after dehydration, differs from that observed in DSC, where Form B undergoes recrystallization with melting at 152.8 °C, whereas Form C shows no recrystallization and melts at 160.8 °C.

3.5. In Vitro Dissolution Tests

In vitro dissolution tests were performed on pure PAS and its three adducts (Form A, B and C) in phosphate buffer (pH 7.4) at 37 °C to evaluate the impact of solid-state modification on the dissolution behavior. The dissolution experiments were performed over a total period of 2 h; however, all samples reached their dissolution plateau within the first 15 min. For clarity, Fig. 8 presents only the first 20 min, which best highlights the differences in dissolution kinetics among the forms. The complete 2 h profiles are provided in the Supplementary material (Fig. S23), confirming that no further changes (*i.e.*, evidence of recrystallization or instability) occur after the plateau is reached. Specifically, all three adducts exhibit faster dissolution kinetics, reaching their plateau concentrations in a shorter time. Among them, Form A (yellow line) is the fastest, achieving complete dissolution within the first 5 min. The hydrated adducts, Form B (green) and Form C (light blue), also outperform pure PAS, though they reach the plateau slightly later than Form A. These data confirm that all three adducts enhance the dissolution rate of PAS.

4. Conclusions

This study comprehensively explored the behaviour and structural diversity of three crystalline adducts formed between *p*-aminosalicylic acid and adenine ($\Delta pK_a = 2.2$): one cocrystal (2:3 ADE:PAS) and two hydrated salts (both 1:1:2 ADE:PAS:H_2O). ADE revealed to be a versatile coformer thanks to the presence of several hydrogen-bond donor and acceptor sites in its molecular structure. By leveraging the region of salt-cocrystal uncertainty, the three forms were successfully and selectively accessed via mechanochemical methods and crystallizations by systematically varying the solvent environment and synthesis conditions. In particular, the application of liquid-assisted grinding, paired with selective solvents, proved to be a robust and reproducible method for directing synthetic outcomes. An in-depth structural and spectroscopic analysis confirmed differences in stoichiometry, hydration state, and intermolecular interactions among the three forms, highlighting how subtle changes in experimental conditions can influence the outcome within the salt–cocrystal continuum. Overall, this work emphasized the importance of the solvent and method selection in directing polymorphic outcomes, particularly when working within the ΔpK_a uncertainty range. We also demonstrated how this chemically ambiguous region, although challenging for prediction, also enables access to multiple forms. The ability to reproducibly isolate multiple solid-state forms from the same molecular components not only enhances our understanding of crystal engineering principles but also opens new possibilities for optimizing pharmaceutical formulations. Furthermore, the findings contribute to the broader field of polymorphism control, offering valuable insights not only in terms of performance enhancement but also with respect to regulatory compliance and intellectual property implications in drug development.

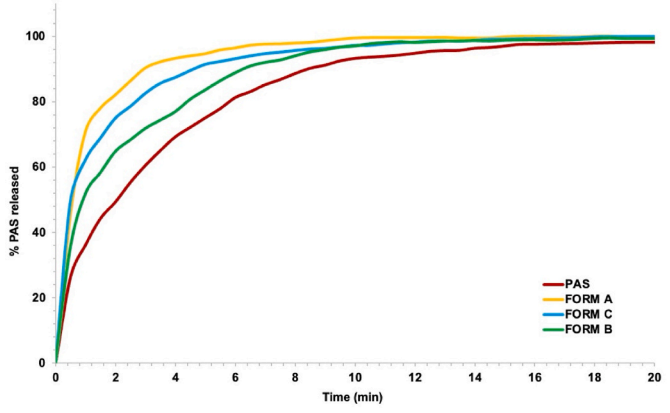

Fig. 8. Enlarged view of the early stage (0–20 min) of the dissolution profiles of pure PAS (red) and the three adducts: Form A (yellow), Form B (green) and Form C (light blue), expressed as % of PAS released. Profiles represent the average of three replicates, with standard deviations not exceeding 5% of the mean value. (For interpretation of the references to color in this figure legend, the reader is referred to the Web version of this article.)

CRediT authorship contribution statement

Beatrice Maiorca: Writing – review & editing, Writing – original draft, Visualization, Methodology, Investigation, Formal analysis, Data curation. **Chiara Sabena:** Writing – review & editing, Writing – original draft, Visualization, Methodology, Investigation, Formal analysis, Data curation. **Emanuele Priola:** Writing – review & editing, Investigation. **Ilenia D'Abbrunzo:** Writing – review & editing, Investigation, Formal analysis. **Beatrice Perissutti:** Writing – review & editing, Supervision. **Roberto Gobetto:** Writing – review & editing, Writing – original draft, Supervision, Resources, Project administration, Methodology, Funding acquisition, Conceptualization. **Michele R. Chierotti:** Writing – review & editing, Writing – original draft, Supervision, Resources, Project administration, Methodology, Funding acquisition, Conceptualization.

Declaration of competing interest

The authors declare the following financial interests/personal relationships which may be considered as potential competing interests: Michele R. Chierotti reports financial support was provided by Ministero dell'Università e della Ricerca. Roberto Gobetto reports financial support was provided by Ministero dell'Università e della Ricerca. Michele R. Chierotti reports financial support was provided by European Union. Roberto Gobetto reports financial support was provided by NODES. If there are other authors, they declare that they have no known competing financial interests or personal relationships that could have appeared to influence the work reported in this paper.

Acknowledgments

Filippo Turchi is sincerely acknowledged for preliminary syntheses of the adducts as part of his master thesis. The authors acknowledge support from the project CH4.0 under the MUR program "Dipartimenti di Eccellenza 2023–2027" (CUP: D13C22003520001), the project FLIPPER (PRIN2022 n. 202224KAX8; CUP D53D23010020006) funded by European Union - Next Generation EU, Mission 4 Component 1, the project NICE (PRIN2020 n. 2020Y2CZJ2; CUP D13C22000440001), and the project "Predire" under the program NODES (CUP:

D17G22000150001).

Appendix A. Supplementary data

Supplementary data to this article can be found online at https://doi.org/10.1016/j.jddst.2025.107762.

Data availability

Data are available in the Supplementary Materials file

References

[1] L.X. Yu, M.S. Furness, A. Raw, K.P.W. Outlaw, N.E. Nashed, E. Ramos, S.P.F. Miller, R.C. Adams, F. Fang, R.M. Patel, F.O. Holcombe, Y. Chiu, A.S. Hussain, Scientific considerations of pharmaceutical solid polymorphism in abbreviated new drug applications, Pharm. Res. 20 (4) (2003) 531–536, https://doi.org/10.1023/A:1023285627778.

[2] Q. Shi, H. Chen, Y. Wang, J. Xu, Z. Liu, C. Zhang, Recent advances in drug polymorphs: aspects of pharmaceutical properties and selective crystallization, Int. J. Pharm. 611 (2022) 121320, https://doi.org/10.1016/j.ijpharm.2021.121320.

[3] R. Prohens, R. Barbas, A. Portell, M. Font-Bardia, X. Alcobé, C. Puigjaner, Polymorphism of cocrystals: the promiscuous behavior of agomelatine, Cryst. Growth Des. 16 (2) (2016) 1063–1070, https://doi.org/10.1021/acs.cgd.5b01628.

[4] S. Aitipamula, P.S. Chow, R.B.H. Tan, Polymorphs and solvates of a cocrystal involving an analgesic drug, ethenzamide, and 3,5-Dinitrobenzoic acid, Cryst. Growth Des. 10 (5) (2010) 2229–2238, https://doi.org/10.1021/cg9015178.

[5] S. Aitipamula, P.S. Chow, R.B.H. Tan, Dimorphs of a 1 : 1 cocrystal of ethenzamide and saccharin: solid-state grinding methods result in metastable polymorph, CrystEngComm 11 (5) (2009) 889–895, https://doi.org/10.1039/B821373A.

[6] S. Aitipamula, P.S. Chow, R.B.H. Tan, Trimorphs of a pharmaceutical cocrystal involving two active pharmaceutical ingredients: potential relevance to combination drugs, CrystEngComm 11 (9) (2009) 1823–1827, https://doi.org/10.1039/B904616J.

[7] D. Braga, G. Palladino, M. Polito, K. Rubini, F. Grepioni, M.R. Chierotti, R. Gobetto, Three polymorphic forms of the Co-Crystal 4,4′-Bipyridine/Pimelic acid and their structural, thermal, and spectroscopic characterization, Chem. Eur J. 14 (32) (2008) 10149–10159, https://doi.org/10.1002/chem.200801051.

[8] D. Bernasconi, S. Bordignon, F. Rossi, E. Priola, C. Nervi, R. Gobetto, D. Voinovich, D. Hasa, N.T. Duong, Y. Nishiyama, M.R. Chierotti, Selective synthesis of a salt and a cocrystal of the ethionamide–salicylic acid system, Cryst. Growth Des. 20 (2) (2020) 906–915, https://doi.org/10.1021/acs.cgd.9b01299.

[9] A. Aramini, G. Bianchini, S. Lillini, S. Bordignon, M. Tomassetti, R. Novelli, S. Mattioli, L. Lvova, R. Paolesse, M.R. Chierotti, M. Allegretti, Unexpected Salt/Cocrystal polymorphism of the Ketoprofen–lysine system: discovery of a new ketoprofen–l-lysine salt polymorph with different physicochemical and pharmacokinetic properties, Pharmaceuticals 14 (6) (2021) 555, https://doi.org/10.3390/ph14060555.

[10] S. Bhandary, K.S.R.N. Mangalampalli, U. Ramamurty, D. Chopra, Crystal structure-mechanical property correlations in N-(3-Ethynylphenyl)-3-Fluorobenzamide polymorphs, Cryst. Growth Des. 18 (1) (2018) 47–51, https://doi.org/10.1021/acs.cgd.7b01432.

[11] E. Joiris, P.D. Martino, C. Berneron, A.-M. Guyot-Hermann, J.-C. Guyot, Compression behavior of orthorhombic paracetamol, Pharm. Res. 15 (7) (1998) 1122–1130, https://doi.org/10.1023/A:1011954800246.

[12] H. Gupta, S. Kumar, S.K. Roy, R.S. Gaud, Patent protection strategies, J. Pharm. BioAllied Sci. 2 (1) (2010) 2, https://doi.org/10.4103/0975-7406.62694.

[13] R. Censi, P. Di Martino, Polymorph impact on the bioavailability and stability of poorly soluble drugs, Molecules 20 (10) (2015) 18759–18776, https://doi.org/10.3390/molecules201018759.

[14] D.D. Gadade, S.S. Pekamwar, Pharmaceutical cocrystals: regulatory and strategic aspects, design and development, Adv. Pharmaceut. Bull. 6 (4) (2016) 479–494, https://doi.org/10.15171/apb.2016.062.

[15] W. Jones, W.D.S. Motherwell, A.V. Trask, Pharmaceutical cocrystals: an emerging approach to physical property enhancement, MRS Bull. 31 (11) (2006) 875–879, https://doi.org/10.1557/mrs2006.206.

[16] S. Aitipamula, R. Banerjee, A.K. Bansal, K. Biradha, M.L. Cheney, A.R. Choudhury, G.R. Desiraju, A.G. Dikundwar, R. Dubey, N. Duggirala, P.P. Ghogale, S. Ghosh, P. K. Goswami, N.R. Goud, R.R.K.R. Jetti, P. Karpinski, P. Kaushik, D. Kumar, V. Kumar, B. Moulton, A. Mukherjee, G. Mukherjee, A.S. Myerson, V. Puri, A. Ramanan, T. Rajamannar, C.M. Reddy, N. Rodriguez-Hornedo, R.D. Rogers, T.N. G. Row, P. Sanphui, N. Shan, G. Shete, A. Singh, C.C. Sun, J.A. Swift, R. Thaimattam, T.S. Thakur, R. Kumar Thaper, S.P. Thomas, S. Tothadi, V. R. Vangala, N. Variankaval, P. Vishweshwar, D.R. Weyna, M.J. Zaworotko, Polymorphs, salts, and cocrystals: what's in a name? Cryst. Growth Des. 12 (5) (2012) 2147–2152, https://doi.org/10.1021/cg3002948.

[17] FDA. Regulatory Classification of Pharmaceutical Co-Crystals Guidance for Industry.

[18] A.V. Yadav, A.S. Shete, A.P. Dabke, P.V. Kulkarni, S.S. Sakhare, Co-Crystals: a novel approach to modify physicochemical properties of active pharmaceutical ingredients, Indian J. Pharmaceut. Sci. 71 (4) (2009) 359–370, https://doi.org/10.4103/0250-474X.57283.

[19] M. Guerain, Y. Guinet, N.T. Correia, L. Paccou, F. Danède, A. Hédoux, Polymorphism and stability of Ibuprofen/Nicotinamide cocrystal: the effect of the crystalline synthesis method, Int. J. Pharm. 584 (2020) 119454, https://doi.org/10.1016/j.ijpharm.2020.119454.

[20] M. Solares-Briones, G. Coyote-Dotor, J.C. Páez-Franco, M.R. Zermeño-Ortega, C. M. de la O Contreras, D. Canseco-González, A. Avila-Sorrosa, D. Morales-Morales, J.M. Germán-Acacio, Mechanochemistry: a green approach in the preparation of pharmaceutical cocrystals, Pharmaceutics 13 (6) (2021) 790, https://doi.org/10.3390/pharmaceutics13060790.

[21] D. Hasa, E. Miniussi, W. Jones, Mechanochemical synthesis of multicomponent crystals: one liquid for one polymorph? A myth to dispel, Cryst. Growth Des. 16 (8) (2016) 4582–4588, https://doi.org/10.1021/acs.cgd.6b00682.

[22] A. Salem, A. Hagymási, B. Vörös-Horváth, T. Šafarik, T. Balić, P. Szabó, F. Gősi, S. Nagy, S. Pál, S. Kunsági-Máté, A. Széchenyi, Solvent dependent 4-Aminosalicylic acid-sulfamethazine Co-Crystal polymorph control, Eur. J. Pharmaceut. Sci. 156 (2021) 105599, https://doi.org/10.1016/j.ejps.2020.105599.

[23] A.J. Cruz-Cabeza, Acid–base crystalline complexes and the pKa rule, CrystEngComm 14 (20) (2012) 6362–6365, https://doi.org/10.1039/C2CE26055G.

[24] S.L. Childs, G.P. Stahly, A. Park, The salt−cocrystal continuum: the influence of crystal structure on ionization state, Mol. Pharm. 4 (3) (2007) 323–338, https://doi.org/10.1021/mp0601345.

[25] A.J. Cruz-Cabeza, M. Lusi, H.P. Wheatcroft, A.D. Bond, The role of solvation in proton transfer reactions: implications for predicting Salt/Co-crystal formation using the ΔpK_a rule, Faraday Discuss 235 (0) (2022) 446–466, https://doi.org/10.1039/D1FD00081K.

[26] M. Quintano, R.T. Moura, E. Kraka, The pKa rule in light of local mode force constants, Chem. Phys. Lett. 826 (2023) 140654, https://doi.org/10.1016/j.cplett.2023.140654.

[27] E.A. Losev, E.V. Boldyreva, A salt or a Co-Crystal – when crystallization protocol matters, CrystEngComm 20 (16) (2018) 2299–2305, https://doi.org/10.1039/C7CE02204B.

[28] S.R. Perumalla, C. Wang, Y. Guo, L. Shi, C.C. Sun, Robust bulk preparation and characterization of sulfamethazine and saccharine salt and cocrystal polymorphs, CrystEngComm 21 (13) (2019) 2089–2096, https://doi.org/10.1039/C8CE01076E.

[29] P. Stainton, T. Grecu, J. McCabe, T. Munshi, E. Nauha, I.J. Scowen, N. Blagden, First comparative study of the three polymorphs of Bis(Isonicotinamide) citric acid cocrystals and the concomitant salt 4-Carbamoylpyridinium citrate isonicotinamide, Cryst. Growth Des. 18 (7) (2018) 4150–4159, https://doi.org/10.1021/acs.cgd.8b00597.

[30] C.L. Jones, J.M. Skelton, S.C. Parker, P.R. Raithby, A. Walsh, C.C. Wilson, L. H. Thomas, Living in the salt-cocrystal continuum: indecisive organic complexes with thermochromic behaviour, CrystEngComm 21 (10) (2019) 1626–1634, https://doi.org/10.1039/C8CE02066C.

[31] D.A. Haynes, W. Jones, W.D.S. Motherwell, Cocrystallisation of succinic and fumaric acids with lutidines: a systematic study, CrystEngComm 8 (11) (2006) 830–840, https://doi.org/10.1039/B610294H.

[32] K.K. Arora, J. PrakashaReddy, V.R. Pedireddi, Pyridine mediated supramolecular assemblies of 3,5-Dinitro substituted benzoic acid, benzamide and benzonitrile, Tetrahedron 61 (45) (2005) 10793–10800, https://doi.org/10.1016/j.tet.2005.08.080.

[33] S. Sedghiniya, J. Soleimannejad, J. Janczak, The salt–cocrystal spectrum in salicylic Acid–adenine: the influence of crystal structure on proton-transfer balance, Acta Crystallogr. C 75 (4) (2019) 412–421, https://doi.org/10.1107/S2053229619003127.

[34] D. Braga, L. Maini, F. Grepioni, Mechanochemical preparation of Co-Crystals, Chem. Soc. Rev. 42 (18) (2013) 7638–7648, https://doi.org/10.1039/C3CS60014A.

[35] N. Schultheiss, A. Newman, Pharmaceutical cocrystals and their physicochemical properties, Cryst. Growth Des. 9 (6) (2009) 2950–2967, https://doi.org/10.1021/cg900129f.

[36] N. Schultheiss, J.-O. Henck, Role of Co-Crystals in the pharmaceutical development continuum, in: J. Wouters, L. Quéré (Eds.), Pharmaceutical Salts and Co-crystals, The Royal Society of Chemistry, 2011, https://doi.org/10.1039/9781849733502-00110, 0.

[37] E. Pindelska, A. Sokal, W. Kolodziejski, Pharmaceutical cocrystals, salts and polymorphs: advanced characterization techniques, Adv. Drug Deliv. Rev. 117 (2017) 111–146, https://doi.org/10.1016/j.addr.2017.09.014.

[38] F. Bravetti, R. Hühn, S. Bordignon, S. Reibeling, M.U. Schmidt, Crystal structure and tautomeric state of pigment red 48:2 from X-Ray powder diffraction and solid-state NMR, Z. Kristallogr. Cryst. Mater. 239 (7–8) (2024) 283–297, https://doi.org/10.1515/zkri-2023-0042.

[39] D. Luedeker, R. Gossmann, K. Langer, G. Brunklaus, Crystal engineering of pharmaceutical Co-crystals: "NMR Crystallography" of Niclosamide Co-Crystals, Cryst. Growth Des. 16 (6) (2016) 3087–3100, https://doi.org/10.1021/acs.cgd.5b01619.

[40] J.A. Fernandes, M. Sardo, L. Mafra, D. Choquesillo-Lazarte, N. Masciocchi, X-Ray and NMR crystallography studies of novel theophylline cocrystals prepared by liquid assisted grinding, Cryst. Growth Des. 15 (8) (2015) 3674–3683, https://doi.org/10.1021/acs.cgd.5b00279.

[41] Q. Zhao, J. Zhang, Y. Jing, J. Xue, J. Liu, J. Qin, Z. Hong, Y. Du, Terahertz and Raman vibrational Spectroscopy detection and structural analysis of acyclovir hydrate polymorphs, Spectrochim. Acta Mol. Biomol. Spectrosc. 338 (2025) 126093, https://doi.org/10.1016/j.saa.2025.126093.

[42] Z. Zhang, S. Li, H. An, R. Tudi, X. Song, M. Zhou, F. Zhang, W. Shi, A. Li, Z. Li, M. Xiang, B. Abulimiti, B. Jin, Research on the cocrystal of methotrexate and histidine based on terahertz spectroscopy and DFT calculations, Chem. Phys. Lett. 878 (2025) 142334, https://doi.org/10.1016/j.cplett.2025.142334.
[43] P. Wang, W. Han, Y. Wu, C. You, C. Zhang, Q. Qu, X. Sun, X. Yang, M. He, Elucidating molecular vibrations within the cocrystal of a nonsteroidal anti-inflammatory drug and amino acid by temperature-dependent terahertz spectroscopy at 2–17 THz: a case Study, Anal. Chem. 97 (38) (2025) 20743–20752, https://doi.org/10.1021/acs.analchem.5c01923.
[44] Y. Du, H. Zhang, J. Xue, H. Fang, Q. Zhang, Y. Xia, Y. Li, Z. Hong, Raman and terahertz spectroscopical investigation of cocrystal Formation process of piracetam and 3-Hydroxybenzoic acid, Spectrochim. Acta Mol. Biomol. Spectrosc. 139 (2015) 488–494, https://doi.org/10.1016/j.saa.2014.11.109.
[45] C.S. Wallace, M.P. Davis, T.M. Korter, Low-Frequency raman spectroscopy of pure and cocrystallized mycophenolic acid, Pharmaceutics 15 (7) (2023) 1924, https://doi.org/10.3390/pharmaceutics15071924.
[46] M.P. Davis, T.M. Korter, Low-frequency vibrational spectroscopy and quantum mechanical simulations of the crystalline polymorphs of the antiviral drug ribavirin, Mol. Pharm. 19 (9) (2022) 3385–3393, https://doi.org/10.1021/acs.molpharmaceut.2c00509.
[47] H. Sun, B. Peng, X. Bai, B. Su, C. Zhang, H. Cui, S. Zhang, K. Li, Spectral characterization and vibrational mode study of cocrystal of Acetaminophen and aspirin based on Terahertz/Raman spectroscopy combined with DFT theory calculation, Results Chem. 16 (2025) 102434, https://doi.org/10.1016/j.rechem.2025.102434.
[48] Y. Jing, Q. Zhao, J. Zhang, J. Xue, J. Liu, J. Qin, Z. Hong, Y. Du, RS, S (+) - and R (−)-Ibuprofen cocrystal polymorphs: vibrational Spectra, XRD measurement and DFT calculation studies, Heliyon 11 (3) (2025) e41986, https://doi.org/10.1016/j.heliyon.2025.e41986.
[49] M. Ge, Y. Wang, J. Zhu, B. Wu, D. Xu, J. Yao, Low-frequency vibrational spectroscopy characteristic of pharmaceutical carbamazepine Co-Crystals with nicotinamide and saccharin, Sensors 22 (11) (2022) 4053, https://doi.org/10.3390/s22114053.
[50] P. Cerreia Vioglio, M.R. Chierotti, R. Gobetto, Pharmaceutical aspects of salt and cocrystal forms of APIs and characterization challenges, Adv. Drug Deliv. Rev. 117 (2017) 86–110, https://doi.org/10.1016/j.addr.2017.07.001.
[51] M.R. Chierotti, R. Gobetto, NMR crystallography: the use of dipolar interactions in polymorph and Co-Crystal investigation, CrystEngComm 15 (43) (2013) 8599, https://doi.org/10.1039/c3ce41026a.
[52] M.R. Chierotti, K. Gaglioti, R. Gobetto, D. Braga, F. Grepioni, L. Maini, From molecular crystals to salt Co-Crystals of barbituric acid via the carbonate Ion and an improvement of the solid state properties, CrystEngComm 15 (37) (2013), https://doi.org/10.1039/C3CE40938D, 7598–7605.
[53] A. Cossard, C. Sabena, G. Bianchini, E. Priola, R. Gobetto, A. Aramini, M. R. Chierotti, Advanced feature analysis for enhancing cocrystal prediction, Chemometr. Intell. Lab. Syst. 257 (2025) 105318, https://doi.org/10.1016/j.chemolab.2025.105318.
[54] WHO Expert Committee on Specifications for Pharmaceutical Preparations, Rev. Inst. Med. trop. S. Paulo 50 (2008), https://doi.org/10.1590/S0036-46652008000300013, 144–144.
[55] S.G. Jivani, V.J. Stella, Mechanism of decarboxylation of *p*-Aminosalicylic acid, J. Pharmaceut. Sci. 74 (12) (1985) 1274–1282, https://doi.org/10.1002/jps.2600741207.
[56] K.V. Drozd, A.N. Manin, A.V. Churakov, G.L. Perlovich, Drug-drug cocrystals of antituberculous 4-Aminosalicylic acid: screening, crystal structures, thermochemical and solubility studies, Eur. J. Pharmaceut. Sci. 99 (2017) 228–239, https://doi.org/10.1016/j.ejps.2016.12.016.
[57] J.T. Carstensen, P. Pothisiri, Decomposition of *p*-Aminosalicylic acid in the solid state, J. Pharmaceut. Sci. 64 (1) (1975) 37–44, https://doi.org/10.1002/jps.2600640107.
[58] P.K. Goswami, R. Thaimattam, A. Ramanan, Multiple crystal forms of P-Aminosalicylic acid: salts, salt Co-Crystal hydrate, Co-Crystals, and Co-Crystal polymorphs, Cryst. Growth Des. 13 (1) (2013) 360–366, https://doi.org/10.1021/cg3015332.
[59] P.K. Goswami, R. Thaimattam, A. Ramanan, Crystal engineering of multicomponent crystal forms of P-Aminosalicylic acid with Pyridine based coformers, Cryst. Growth Des. 16 (3) (2016) 1268–1281, https://doi.org/10.1021/acs.cgd.5b01308.
[60] T. Yoshimoto, M. Seki, H. Okabe, N. Matsuda, D. Wu, M. Futamata, Three distinct adsorbed states of adenine on gold nanoparticles depending on pH in aqueous solutions, Chem. Phys. Lett. 786 (2022) 139202, https://doi.org/10.1016/j.cplett.2021.139202.
[61] S.S. Kumar, A.A. Nangia, Solubility comparison of neutral and zwitterionic polymorphs, Cryst. Growth Des. 14 (4) (2014) 1865–1881, https://doi.org/10.1021/cg5000205.
[62] Y. Du, H.X. Fang, Q. Zhang, H.L. Zhang, Z. Hong, Spectroscopic investigation on cocrystal formation between adenine and fumaric acid based on infrared and raman techniques, Spectrochim. Acta Mol. Biomol. Spectrosc. 153 (2016) 580–585, https://doi.org/10.1016/j.saa.2015.09.020.
[63] D. Lv, W. Nong, Y. Guan, Edible ligand-metal-organic frameworks: synthesis, structures, properties and applications, Coord. Chem. Rev. 450 (2022) 214234, https://doi.org/10.1016/j.ccr.2021.214234.
[64] M. Byres, P.J. Cox, G. Kay, E. Nixon, Supramolecular structures of six adenine-carboxylic acid complexes, CrystEngComm 11 (1) (2009) 135–142, https://doi.org/10.1039/B811243F.
[65] C. McHugh, A. Erxleben, Supramolecular structures and tautomerism of carboxylate salts of adenine and pharmaceutically relevant N6-Substituted adenine, Cryst. Growth Des. 11 (11) (2011) 5096–5104, https://doi.org/10.1021/cg201007m.
[66] G.M. Sheldrick, A short history of SHELX, Acta Crystallogr. A 64 (1) (2008) 112–122, https://doi.org/10.1107/S0108767307043930.
[67] G.M. Sheldrick, SHELXT - integrated space-group and crystal-structure determination, Acta Crystallogr A Found Adv 71 (Pt 1) (2015) 3–8, https://doi.org/10.1107/S2053273314026370.
[68] O.V. Dolomanov, L.J. Bourhis, R.J. Gildea, J.A.K. Howard, H. Puschmann, OLEX2: a complete structure solution, refinement and analysis program, J. Appl. Crystallogr. 42 (2009) 339–341, https://doi.org/10.1107/S0021889808042726FILE.
[69] C.F. Macrae, I.J. Bruno, J.A. Chisholm, P.R. Edgington, P. McCabe, E. Pidcock, L. Rodriguez-Monge, R. Taylor, J. Van De Streek, P.A. Wood, *Mercury CSD 2.0* – new features for the visualization and investigation of crystal structures, J. Appl. Crystallogr. 41 (2) (2008) 466–470, https://doi.org/10.1107/S0021889807067908.
[70] A. Gavezzotti, Are crystal structures predictable? Acc. Chem. Res. 27 (10) (1994) 309–314, https://doi.org/10.1021/ar00046a004.
[71] P.R. Spackman, M.J. Turner, J.J. McKinnon, S.K. Wolff, D.J. Grimwood, D. Jayatilaka, M.A. Spackman, CrystalExplorer: a program for Hirshfeld surface analysis, visualization and quantitative analysis of molecular crystals, J. Appl. Crystallogr. 54 (3) (2021) 1006–1011, https://doi.org/10.1107/S1600576721002910.
[72] C.F. Mackenzie, P.R. Spackman, D. Jayatilaka, M.A. Spackman, CrystalExplorer model energies and energy frameworks: extension to metal coordination compounds, organic salts, solvates and open-shell systems, IUCrJ 4 (5) (2017) 575–587, https://doi.org/10.1107/S205225251700848X.
[73] E. Irrou, Y.A. Elmachkouri, A. Oubella, H. Ouchtak, S. Dalbouha, J.T. Mague, T. Hökelek, L. El Ghayati, N.K. Sebbar, M.L. Taha, Crystal structure determination, Hirshfeld surface, crystal void, inter-molecular inter-action energy analyses, as well as DFT and energy framework calculations of 2-(4-Oxo-4,5-Di-hydro-1H-Pyrazolo[3,4-d]Pyrimidin-1-Yl)Acetic acid, Acta Crystallogr. 78 (9) (2022) 953–960, https://doi.org/10.1107/S2056989022008489.
[74] M.A. Spackman, J.J. McKinnon, D. Jayatilaka, Electrostatic potentials mapped on hirshfeld surfaces provide direct Insight into intermolecular interactions in crystals, CrystEngComm 10 (4) (2008) 377–388, https://doi.org/10.1039/B715227B.
[75] T. Friščić, Supramolecular concepts and new techniques in mechanochemistry: cocrystals, cages, rotaxanes, open metal–organic frameworks, Chem. Soc. Rev. 41 (9) (2012) 3493–3510, https://doi.org/10.1039/C2CS15332G.
[76] D. Hasa, G. Schneider Rauber, D. Voinovich, W. Jones, Cocrystal formation through mechanochemistry: from neat and liquid-assisted grinding to polymer-assisted grinding, Angew. Chem. Int. Ed. 54 (25) (2015) 7371–7375, https://doi.org/10.1002/anie.201501638.
[77] F. Fischer, G. Scholz, S. Benemann, K. Rademann, F. Emmerling, Evaluation of the formation pathways of cocrystal polymorphs in liquid-assisted syntheses, CrystEngComm 16 (35) (2014) 8272–8278, https://doi.org/10.1039/C4CE00472H.
[78] S. Bordignon, P. Cerreia Vioglio, C. Bertoncini, E. Priola, R. Gobetto, M. R. Chierotti, Pseudopolymorphism driven by stoichiometry and Hydrated/Anhydrous reagents: the riveting case of methyl gallate·l-proline, Cryst. Growth Des. 21 (12) (2021) 6776–6785, https://doi.org/10.1021/acs.cgd.1c00680.
[79] R.L. Maynard, The Merck Index: 12th Edition 1996, Occup. Environ. Med. 54 (4) (1997) 288.
[80] Z. Zhang, J. Fang, Y. Bo, J. Xue, J. Liu, Z. Hong, Y. Du, Terahertz and raman spectroscopic investigation of anti-tuberculosis drug-drug cocrystallization involving 4-Aminosalicylic acid and pyrazinamide, J. Mol. Struct. 1227 (2021) 129547, https://doi.org/10.1016/j.molstruc.2020.129547.
[81] R.P. Lopes, R. Valero, J. Tomkinson, M.P.M. Marques, L.A.E. Batista de Carvalho, Applying vibrational spectroscopy to the Study of nucleobases – adenine as a case-study, New J. Chem. 37 (9) (2013) 2691–2699, https://doi.org/10.1039/C3NJ00445G.
[82] T.G. Burova, V.V. Ermolenkov, G.N. Ten, R.S. Shcherbakov, V.I. Baranov, I. K. Lednev, Raman spectroscopic study of the tautomeric composition of adenine in water, J. Phys. Chem. A 115 (38) (2011) 10600–10609, https://doi.org/10.1021/jp2033033.
[83] B. Saifullah, M.Z. Hussein, S.H. Hussein-Al-Ali, P. Arulselvan, S. Fakurazi, Sustained release formulation of an anti-tuberculosis drug based on para-amino salicylic acid-zinc layered hydroxide nanocomposite, Chem. Cent. J. 7 (1) (2013) 72, https://doi.org/10.1186/1752-153X-7-72.
[84] N.C. Gonnella, J.D. Roberts, Studies of the tautomerism of purine and the protonation of purine, and its 7- and 9-Methyl derivatives, by Nitrogen-15 nuclear magnetic resonance spectroscopy, J. Am. Chem. Soc. 104 (11) (1982) 3162–3164, https://doi.org/10.1021/ja00375a038.
[85] J. Prashanth, A.S. Devi, A.O. Surov, A.P. Voronin, A.V. Churakov, G.L. Perlovich, S. Balasubramanian, Understanding the thermal stability of apalutamide crystalline solvates through crystal structure analyses and computational studies,

CrystEngComm 24 (19) (2022) 3511–3528, https://doi.org/10.1039/D2CE00216G.

[86] M.K. Rotich, B.D. Glass, M.E. Brown, Thermal studies on some substituted aminobenzoic acids, J. Therm. Anal. Calorim. 64 (2) (2001) 681–688, https://doi.org/10.1023/A:1011584125859.

[87] G. Verreck, A. Decorte, K. Heymans, J. Adriaensen, D. Liu, D. Tomasko, A. Arien, J. Peeters, G. Van den Mooter, M.E. Brewster, Hot stage extrusion of *p*-Amino salicylic acid with EC using CO2 as a temporary plasticizer, Int. J. Pharm. 327 (1) (2006) 45–50, https://doi.org/10.1016/j.ijpharm.2006.07.024.